Materials Today Energy 40 (2024) 101497

Contents lists available at ScienceDirect

Materials Today Energy

journal homepage: www.journals.elsevier.com/materials-today-energy/

Enhancing lithium-sulfur battery performance through electronic/ionic co-conductive multi-walled carbon nanotubes/lithium lanthanum titanium oxide separator modification

Shanshan Liang [a, b, **], Susana Chauque [a], Marco Ricci [a, b], Remo Proietti Zaccaria [a, c, *]

[a] Istituto Italiano di Tecnologia, Via Morego 30, 16163, Genova, Italy
[b] Department of Chemistry and Industrial Chemistry, University of Genova, Via Dodecaneso 31, 1, 16146, Genova, Italy
[c] Department of Physics, Shaoxing University, 312000, Shaoxing, China

ARTICLE INFO

Article history:
Received 10 October 2023
Received in revised form
23 December 2023
Accepted 4 January 2024
Available online 9 January 2024

Keywords:
Shuttle effect
separator
high-performance batteries
1D conductors
elecronic and ionic conductors

ABSTRACT

As one of the most promising energy storage devices, lithium-sulfur batteries (LSBs or Li-S batteries) are still facing obstacles due to the notorious shuttling of soluble polysulfide intermediates, accompanied by low S utilization, corrosion of the lithium anode, and rapid capacity fading, leading to a short cycling life. To overcome these issues and achieve high-performance LSBs, we introduce a modified separator composed of multi-walled carbon nanotubes/lithium lanthanum titanium oxide (MWCNTs/LLTO). The proposed MWCNTs/LLTO-modified separator improves the redox reaction kinetics from soluble higher-order lithium polysulfides to insoluble lower-order ones and ultimately to Li_2S, thereby reducing the polysulfides dissolved in the electrolyte. It also serves as a physical barrier to adsorb polysulfides, efficiently preventing their diffusion from the cathode to the anode. LSBs adopting the MWCNTs/LLTO-modified separator exhibit higher ionic and electronic conductivity than their un-modified counterparts, leading to an initial specific capacity of 1496 mA/h/g (~90% of the theoretical capacity) at 0.1 C, excellent rate capability performance, and a remarkable capacity retention of 80% after 200 cycles. Furthermore, the cells with S loading reaching up to 4.18 mg/cm^2 further confirmed the beneficial impact of the MWCNTs/LLTO-modified separator.

1. Introduction

Lithium-sulfur batteries (LSBs) with an extremely high theoretical specific capacity of 1675 mA/h/g and an energy density of 2600 Wh/kg are regarded as one of the most promising candidates for the next generation of rechargeable batteries [1–4]. Besides, S is low-cost, environment-friendly, and abundant in nature, making this material extremely attractive. However, the intermediate lithium polysulfides (LiPSs) formed during the discharge process are soluble in conventional liquid electrolytes [5], determining their diffusion between cathode and anode through the microporous separator during cycling. This leads to problems such as diminished S utilization, loss of active material, corrosion of the metallic lithium anode, and swift capacity deterioration, ultimately resulting in a limited lifespan [6–8]. This well-known phenomenon, often termed as the shuttle effect, stands as a significant barrier that hinders the practical implementation of LSBs [9].

Nowadays, various strategies addressing the shuttle effect in LSBs have been developed, such as the introduction of innovative cathode designs [10,11], electrolyte compositions [12–15], separator modifications [16,17], and protecting the lithium metal anode [18,19]. Among them, the rational design of a functional separator plays an important role in improving the performance of LSBs. Previous studies have shown that coating the separator with carbonaceous materials such as graphene [20] or carbon nanofibers [21], could possibly immobilize and recycle soluble polysulfides. Furthermore, coating separators with some transition metal compounds, like oxides [22], sulfides [23,24], nitrides [25,26], and heterostructures [27,28], could provide better inhibition of the shuttle effect owing to the strong chemical interaction between polysulfides and transition metal ions and accelerate the polysulfide conversion during charge/discharge processes by acting as catalysts [29]. However, transition metal compounds have limited electrical conductivity, resulting in a negative impact on the

* Corresponding author.
** Corresponding author.
E-mail addresses: shanshan.liang@iit.it (S. Liang), remo.proietti@iit.it (R.P. Zaccaria).

https://doi.org/10.1016/j.mtener.2024.101497

conversion of polysulfides. Although metal sulfides are more conductive than metal oxides, their combination with conductive carbon materials is still needed to further reduce the internal electrical resistance [30]. In general, a separator made only of transition metal compounds is incapable to meet the requirements for high-performance LSBs. Therefore, multifunctional materials with reasonable design and easy preparation bring more possibilities in the development of more efficient LSBs [31–33].

Here, we develop an electronic and ionic coconductive multi-walled carbon nanotubes (MWCNTs)/lithium lanthanum titanate (LLTO)-modified separator to be employed in LSBs. Owing to the filament-like morphology and the electrical conductivity of MWCNTs, this material can operate as a spontaneous bridge, linking the retention of LiPSs inside the coating to the S cathode to activate the "dead S′ in the electrochemical reaction [34]. On the other hand, perovskite-type $La_{0.56}Li_{0.33}TiO_3$ (LLTO) is known as a good ionic conductor with high thermal stability [35–37]. The fast Li^+ transport in LLTO (ABO_3 perovskite structure) is primarily determined by the vacancies occupying the A position (Li-rich layer in Fig. 1a) [38]. The existence of these vacancies increases the interaction probability between the polysulfide species and sulfiphilic Ti^+, further transforming into thiosulfate and polythionate intermediates [39] (Fig. 1b), in turn reducing the shuttle effect. Therefore, this electronic and ionic co-conductive coating composed by MWCNTs and LLTO is expected to improve both the electronic and ionic conductivity inside the LSBs, thereby accelerating the redox reaction kinetics on the S cathode. Furthermore, the coating can also inhibit the shuttle effect via physical adsorption and chemisorption of polysulfide species, reducing the irreversible loss of active materials and the corrosion of lithium metal (Fig. 1c). As a result of the improved kinetics, LSBs with MWCNTs/LLTO-modified separators not only deliver a higher specific capacity but also a large rate capability.

2. Experimental section

2.1. Preparation of multi-walled carbon nanotubes/lithium lanthanum titanium oxide-modified separator

Both the LLTO ($La_{0.56}Li_{0.33}TiO_3$) powder and the MWCNTs were purchased from Sigma. To fabricate the MWCNTs/LLTO-modified separator, a commercial polypropylene membrane (Celgard 2400) was coated on one side by a MWCNTs/LLTO slurry by using the doctor blade method. The slurry was prepared by mixing LLTO, MWCNTs, and polyvinylidene fluoride (PVDF, Kynar® HSV 900) in a weight ratio of 8:1:1 using N-Methyl-2-pyrrolidone (NMP) as the solvent and stirring for 6 h. After coating the Celgard separator, it was carefully dried at 60 °C overnight, and then it was cut into disks with a diameter of 18 mm. For comparison purposes, LLTO-coated Celgard, MWCNTs-coated Celgard, and pristine Celgard were used as reference separators.

2.2. Preparation of S-based cathode and Li-S cells

A S/MWCNTs composite material was prepared by the typical melting method [40]. The S powders, purified by sublimation, were mixed with MWCNTs in an agate mortar in a weight ratio of 4:1. Then the S/MWCNTs mixture was sealed in a polytetrafluoroethylene (PTFE) container under an inert atmosphere, and a thermal treatment of 155 °C for 12 h was applied. Fig. S1 shows the exact S content of 80.12% in the S/MWCNT composite after treatment. Afterward, the as-prepared active material, Super-P carbon black, and polyvinylidene fluoride binder in a weight ratio of 8:1:1 were mixed using N-Methyl-2-pyrrolidone as solvent and maintained under stirring for 6 h in order to obtain a homogeneous slurry. The slurry was then coated by the doctor-blade technique on a commercial aluminum (Al) foil and dried at 40 °C overnight. The

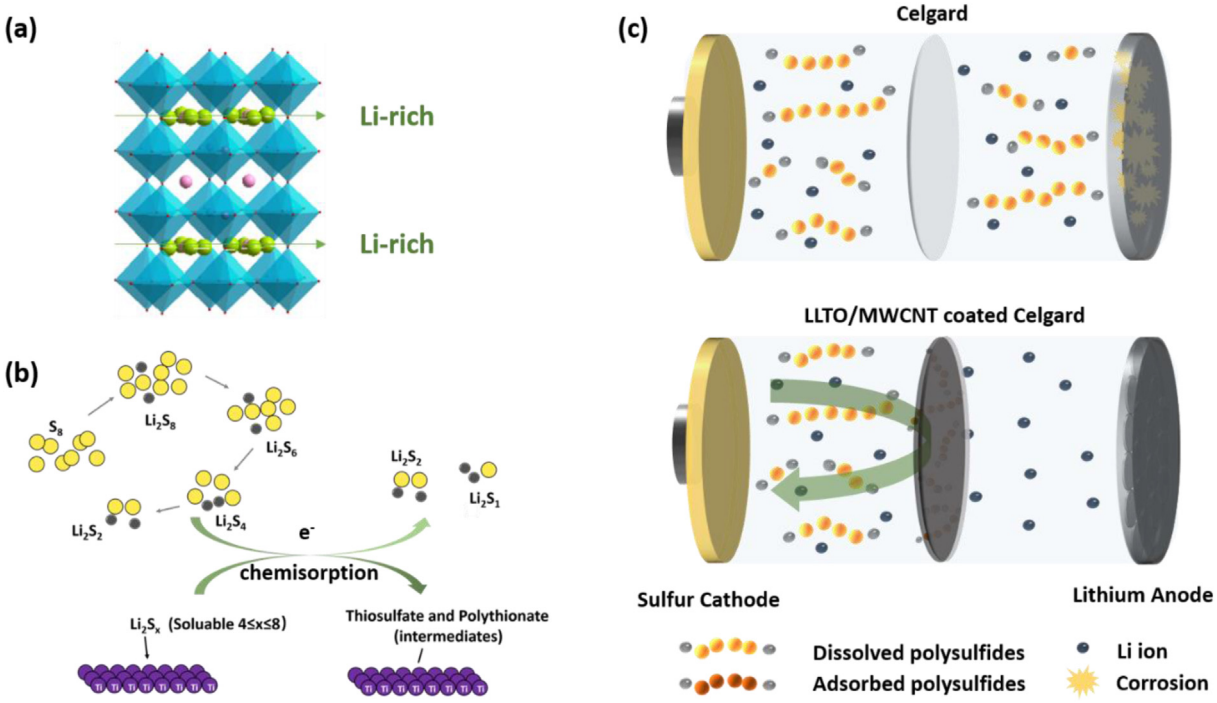

Fig. 1. Schematic illustration of (a) the lithium-ion transport pathway in LLTO. (b) Lithium polysulfide conversion. (c) The role of separators in inhibiting polysulfide in LSBs, comparing a conventional Celgard separator (top) with an improved MWCNTs/LLTO-coated separator (bottom). LLTO, lithium lanthanum titanate; LSBs, lithium-sulfur batteries; MWCNTs, multi-walled carbon nanotubes.

dried electrode sheet was cut into disks with a diameter of 12 mm, and its average S mass loading was 2 mg/cm^2. Furthermore, cathodes with a S loading of around 4.18 mg/cm^2 were prepared by the same method.

CR2032-type coin cells were assembled in an argon-filled glove box (Mbraun), where oxygen and water contents were less than 0.1 ppm. The as-prepared S electrodes were used as the cathode, while lithium metal chips (16 mm in diameter) were used as the anode. The commercial ether-based electrolyte from Tob New Energy Technology Co., consisting of a solution of 1 M lithium bis(-trifluoromethylsulfonyl)imide (LiTFSI) and 2.0 wt% lithium nitrate ($LiNO_3$) in 1,3-dioxolane (DOL) and 1,2-dimethoxyethane (DME) (1:1 by volume), was employed with the electrolyte-to-S ratios (E/S) of 12 μL/mg and 6 μL/mg for the configurations with S loadings of 2 mg/cm^2 and 4.18 mg/cm^2, respectively.

2.3. Materials characterization

The crystal structure of the LLTO sample was characterized by X-ray diffraction (XRD) using a Malvern Panalytical Empyrean instrument equipped with a Cu Kα source. The transmission electron microscopy (TEM) images were acquired with a FEI Tecnai G2 F20 TWIN TMP TEM/STEM system. The morphology and composition were examined by scanning electron microscopy (SEM) analysis and energy dispersive spectroscopy (EDS) on the JEOL JSM-6490LA SEM. The chemical compositions were determined by X-ray photoelectron spectroscopy (XPS) using a Kratos Axis Ultra analyzer with binding energy (BE) calibrated to the C 1s peak (284.58 eV).

2.4. Polysulfides adsorption tests

A polysulfide solution of 0.05 M Li_2S_6 was prepared through a reaction between lithium sulfide (Li_2S) and elemental S (molar ratio 3:1) in dioxolane/ dimethoxyethane (volume ratio of 1:1) by stirring for 24 h at 60 °C in an argon-filled glove box. Subsequently, LLTO and MWCNTs were separately added to the polysulfide solution. After standing for 12 h, a UV−vis absorption spectrophotometer (Varian Cary 300) was used to record the UV−visible absorption of ten-fold diluted solutions.

An H-type electrolytic cell was used to investigate polysulfide diffusion. The separator was positioned between the two branch tubes, containing 0.05 M Li_2S_6 in the electrolyte solution (left side) and the colourless electrolyte solution (right side).

2.5. Electrochemical characterization

Galvanostatic charge/discharge (GCD) tests were carried out at a current ranging from 0.1 C to 5 C (1C = 1675 mA/g) in the potential range of 1.7−2.8 V versus Li/Li$^+$. Electrochemical impedance spectroscopy (EIS) experiments were tested in the frequency range of 10 kHz−100 mHz before and after cycling at 0.5 C. Cyclic voltammetry (CV) tests of the Li-S cells were performed at different scan rates from 0.05 mV/s to 0.25 mV/s in the potential range of 1.5−3.0 V versus Li/Li$^+$. The lithium-ion diffusion coefficient D_{Li}^+, which describes the migration rate of lithium ions within the battery during charging and discharging processes, was calculated by the Randles−Sevcik equation [41]:

$$I_p = 2.69 \times 10^5 \cdot n^{3/2} \cdot A \cdot D_{Li^+}^{1/2} \cdot C_{Li^+} \cdot v^{1/2} \quad (1)$$

where I_p is the peak current (A), n is the number of electrons involved in the reaction, A is the electrode surface area (cm^2), C is the Li-ion concentration in the active material (mol cm^{-3}), and v is the scan rate (V s^{-1}). Considering C, n, and A as constants, the value of D_{Li}^+ (calculated in cm^2 s^{-1}) is proportional to the slope of I_p ($dI_p/dv^{1/2}$).

Additionally, the Li-ion transport number t_{Li+}, which quantifies the amount of the total electric current carried by the lithium ions, was obtained from EIS and chronopotentiometry measurements [42]. Li|Li symmetrical cells were assembled by placing a separator between two disks of metallic lithium and tested with a step potential of 10 mV for 120 min until stabilization. Afterward, EIS experiments were performed by applying 10 mV of signal amplitude in the frequency range of 10 kHz−100 mHz before and after the direct current polarization. According to the Bruce−Vincent equation, the Li-ion transport number can be calculated as follows [42]:

$$t_{Li+} = \frac{I_{ss}\,(V - I_0 R_0)}{I_0\,(V - I_{ss} R_{SS})} \quad (2)$$

where t_{Li+} is the Li-ion transport number, I_{ss} and I_0 are the steady-state and initial current values, respectively, V is the applied polarization potential of 10 mV, R_0 is the initial resistance, and R_{ss} is the resistance at the steady state.

3. Results and discussion

The materials employed for the fabrication of the separators as well as the separators themselves were analyzed by addressing their chemical structure, morphology, and electrochemical properties.

The X-ray diffraction pattern of LLTO (Fig. S2a) closely resembles the characteristic peaks of the tetragonal $Li_{0.33}La_{0.557}TiO_3$ (PDF 87−0935) structure. The insets depict the morphology of LLTO and the corresponding selected area electron diffraction (SAED) pattern, which are consistent with a polycrystalline structure with a tetragonal unit cell. To obtain more structural information about the pristine LLTO material, the zoomed-in area high-resolution transmission electron microscopy (HRTEM) micrograph presented in Fig. S2b was obtained after being frequency-filtered using the average background subtraction filter (ABSF). The extended single-crystal regions are consistent with the (001) direction of the tetragonal $Li_{0.33}La_{0.557}TiO_3$ structure in the LLTO fragments. Similarly, for the MWCNT material, its HRTEM micrograph and spacing (0.334 nm) are shown in Fig. S3. This structure provides more adsorption sites and ensures good electron conduction in the modified separator.

The SEM micrographs shown in Figs. 2a and b depict the surface and cross-section of the separator coated with MWCNTs/LLTO. In particular, the cross-sectional micrograph (Fig. 2b) reveals the successive and relatively dense coating layer, with a thickness of approximately 10 μm. The elemental mappings of La, Ti, and C (Fig. 2c−e) disclose the evenly dispersed LLTO particles among the matrix of interconnected MWCNTs.

Additionally, the folding and unfolding experiments (Fig. S4) served to demonstrate that the MWCNTs/LLTO-coated separator is remarkably robust, which could be beneficial for large-scale fabrication. Furthermore, due to the high thermal stability of both LLTO and MWCNTs, it was demonstrated that the modified separator could withstand temperatures as high as 150 °C (Fig. S5), much better than a bare Celgard separator. This feature is essential for averting thermal failure in batteries caused by overcharging.

To evaluate the adsorption capability of MWCNTs and LLTO towards polysulfides, the UV−Vis spectra were measured after immersing separately LLTO and MWCNTs samples into Li_2S_6 solution (0.05 M) for 12 h. In Fig. 3a, the absorption peaks around 260 nm and 280 nm are attributed to S_6^{2-} species. Another peak at around 410 nm is observed due to the presence of S_4^{2-} species [43].

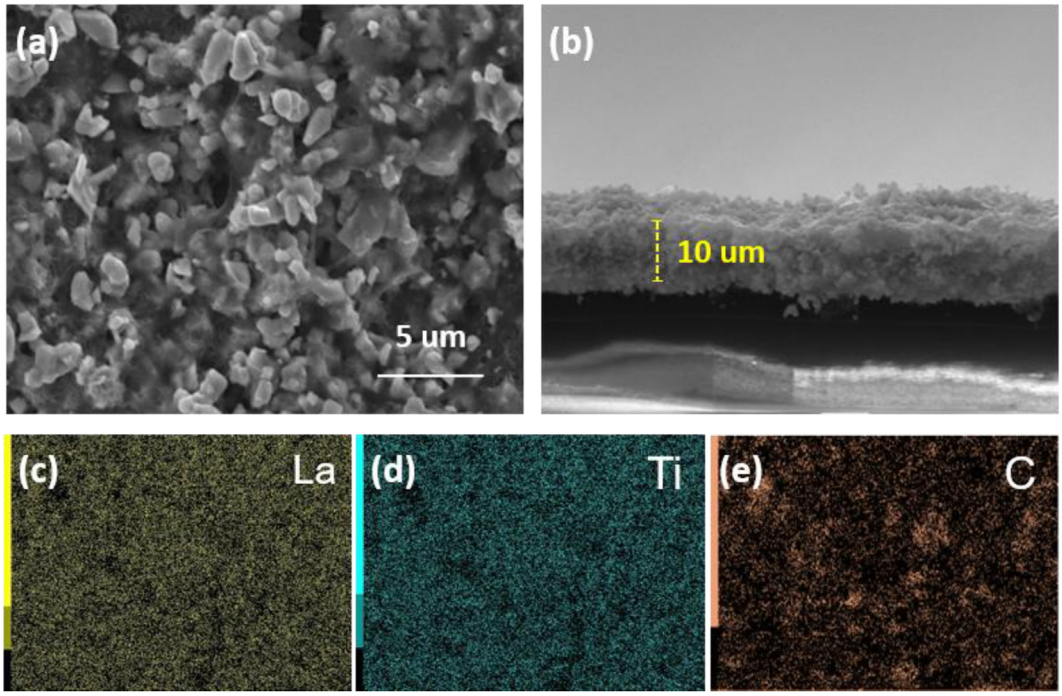

Fig. 2. SEM micrographs of MWCNTs/LLTO-coated separator. (a) Top view, (b) cross-sectional view, and (c-e) elemental mappings of La, Ti, and C. SEM, scanning electron microscopy; MWCNTs/LLTO, multi-walled carbon nanotubes/lithium lanthanum titanium odxide.

All the absorption signals decrease in the solutions containing LLTO or MWCNTs, hence demonstrating significant adsorption capabilities towards polysulfides of these two materials. In this respect, the inset illustrates the colors associated with the different samples. Indeed, when the red Li_2S_6 solution is combined with LLTO or MWCNTs samples, it becomes significantly lighter, confirming that both LLTO and MWCNTs are capable of effectively trapping polysulfides.

Besides, the diffusion of LiPSs in the electrolyte was also investigated. Fig. S6a describes the color changes of an H-type electrolytic cell within 12 h, containing Li_2S_6 in the electrolyte solution (left side) and the colorless electrolyte solution (right side). For the commercial Celgard separator, the electrolyte solution in the right tube turned yellow just after 2 h, to assume a bright yellow color after 12 h (Fig. S6a). In contrast, when the MWCNTs/LLTO-coated separator was considered, no color change was observed for 6 h, and only a faint yellow color appeared after 12 h (Fig. S6b). These results suggest that the MWCNTs/LLTO-coated separator can effectively diminish the penetration of LiPSs, which is of great relevance for suppressing the shuttle effect in LSBs.

Another parameter that was evaluated is the Li-ion transport number (t_{Li+}), which represents the percentage of the current carried by the Li-ions in the electrolyte during the charge and discharge processes [44]. According to the Bruce—Vincent equation (Eq. (2)), t_{Li+} is calculated from the initial and steady-state values of the current together with the resistance values as shown in the EIS tests depicted in the insets of Fig. 3b—c and Figs. S7a and b. When a pristine Celgard separator is employed (Fig. 3b), t_{Li+} is found to be 0.35 and to grow up to 0.37 after the modification with MWCNTs (Fig. S7a). In contrast, the t_{Li+} of LLTO (Fig. S7b) and MWCNTs/LLTO-modified Celgard (Fig. 3c) are 0.40 and 0.42, respectively, indicating that the addition of LLTO as a fast Li-ion conductor could significantly enhance the Li-ion transport capability of the separator.

In order to address the electrochemical effectiveness of the illustrated solutions, cyclic voltammetry tests were also carried out at a scan rate of 0.05 mV/s, as shown in Fig. 3d. It was observed that the cells with MWCNTs-modified separators, including both MWCNTs and MWCNTs/LLTO, exhibited a higher response in the peak current owing to the excellent electrical conductivity of the MWCNTs material. Furthermore, the presence of LLTO (for both LLTO and MWCNTs/LLTO-modified Celgard separators), when compared to the CV curves associated with a pristine Celgard separator, showed a shifting of the reduction peaks towards higher potential, while the oxidation peaks were shifted towards lower potential. Overall, the cells containing the MWCNTs/LLTO-modified separator demonstrated superior reversibility and lower polarization. In addition, the CV tests at different scan rates were carried out from 0.05 mV/s to 0.25 mV/s. The redox peaks (two cathodic peaks C_1 and C_2, and one anodic peak A) for the cells with MWCNTs/LLTO-modified separator (Fig. 3f) show a smaller potential shift than the cells with pristine Celgard separator (Fig. 3e), with MWCNTs-modified separator (Fig. S8a), and with LLTO-modified separator (Fig. S8a). These results suggest that an electronic and ionic co-conductive MWCNTs/LLTO coating could effectively accelerate the redox kinetics of LSBs.

The lithium-ion diffusion coefficient D_{Li}^{+} could more precisely describe the Li-ion diffusion velocity in LSBs [41]. Based on the Randles-Sevick equation, the value of D_{Li}^{+} is proportional to the slope of I_p ($dI_p/dv^{1/2}$). Therefore, the linear relationships between the peaks current and the square root of the scan rate are fitted to compare the D_{Li}^{+} at various redox positions (i.e., C_1, C_2, and A), as shown in Fig. 3g—i. The values of the D_{Li}^{+} are calculated and listed in Table S1. All the cells with the modified separator display a higher D_{Li}^{+} value than the cells with a pristine Celgard separator, suggesting that employing a good electronic or ionic conductor is beneficial for achieving high D_{Li}^{+} values. In particular, the cells with MWCNTs show even a higher lithium-ion diffusion coefficient than the cells with LLTO, hence underlying the importance of electronic conductivity over fast lithium-ion conductivity for achieving high D_{Li}^{+} coefficients. Indeed, we argue that the trapped

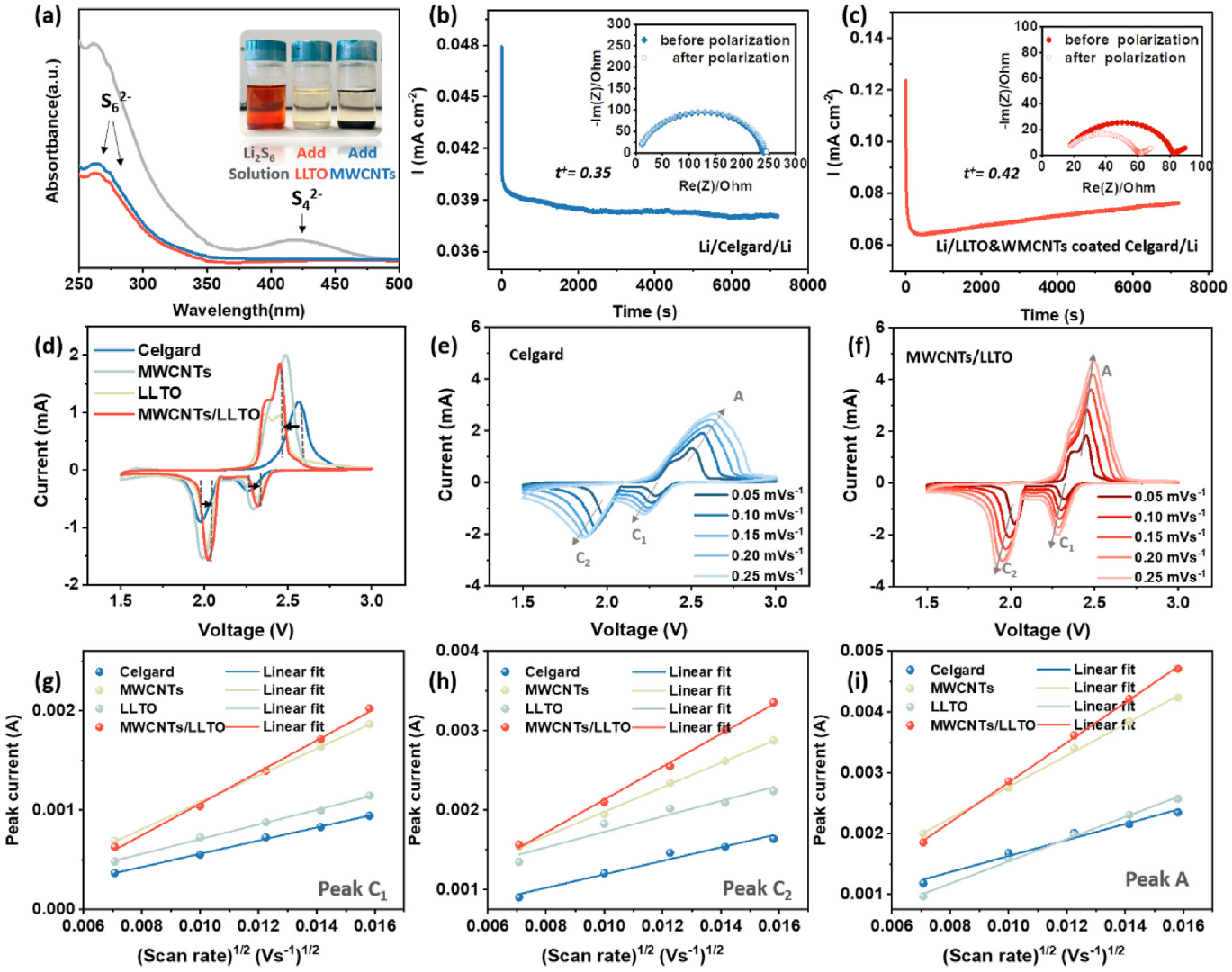

Fig. 3. (a) UV–Vis absorption spectra of different samples (Li_2S_6 black line, Li_2S_6+LLTO red line, Li_2S_6+MWCNTs blue line) and their optical photo in the inset. Current density under polarization potential and the corresponding EIS plots of symmetrical cells with (b) pristine Celgard and (c) MWCNTs/LLTO-modified separators. (d) CV curves of different cells at the scan rate of 0.05 mV s^{-1} in the potential range of 1.5–3.0 V. CV curves of Li-S cells with (e) pristine Celgard and (f) MWCNTs/LLTO-modified separators at scan rates ranging from 0.05 mV s^{-1} to 0.25 mV s^{-1}. The linear fits between the peaks current and the square root of the scan rate of different cells are shown in (g), (h), and (i) for the cathodic peaks C_1, C_2, and the anodic peak A, respectively. EIS, electrochemical impedance spectroscopy; MWCNTs/LLTO, multi-walled carbon nanotubes/lithium lanthanum titanium oxide; CV, cyclic voltammetry.

polysulfides could more easily acquire/release electrons during the redox process owing to the presence of electronically conductive MWCNTs in the separator, thus mitigating a possible accumulation of insoluble Li_2S_2/Li_2S.

Finally, the cells containing the MWCNTs/LLTO-modified separator, therefore combining together the advantages of good electronic and ionic conductors, exhibit the maximum D_{Li}^{+} values for all three redox peaks: A ($D_{Li}^{+} = 3.01 \times 10^{-7}$ cm^2/s), C_1 ($D_{Li}^{+} = 7.10 \times 10^{-8}$ cm^2/s) and C_2 ($D_{Li}^{+} = 1.20 \times 10^{-7}$ cm^2/s). These results suggest that MWCNTs/LLTO-coated separators could improve both Li^+ and electron transfer, thereby significantly accelerating the lithium-ion diffusion kinetics during both the charge and discharge processes and further enhancing the electrochemical performances of LSBs.

The rate capability and the galvanostatic cycling performance on Li–S cells employing the modified separators were investigated within a potential range of 1.7–2.8 V vs. Li/Li^+ (Fig. 4).

The specific discharge capacities of Li-S cells employing pristine Celgard, MWCNTs, LTTO, and MWCNTs/LTTO-modified separators are depicted in Fig. 4a for the C-rates 0.1C, 0.2C, 0.5C, 1C, 2C, and 5C. In particular, when the MWCNTs/LLTO-modified separator is considered, the corresponding specific capacities are 1388, 1211, 1097, 1032, 833, and 662 mA/h/g, respectively. Importantly, these values are higher than for Li-S cells employing pristine Celgard. Indeed, the difference in specific capacities is more obvious at high current densities, 662 against 45 mA/h/g at 2 C and even more striking at 5 C, where the Li-S cells with pristine Celgard separator fail to work.

The superiority of the rate performance of the MWCNTs/LTTO solution over other approaches, especially at high current densities, is schematized in Table S2. Furthermore, when compared to the cells containing either LLTO or MWCNTs-modified separators, the specific capacity is also enhanced. Specifically, for the initial cycle, the galvanostatic charge/discharge profiles are displayed in Fig. 4b,

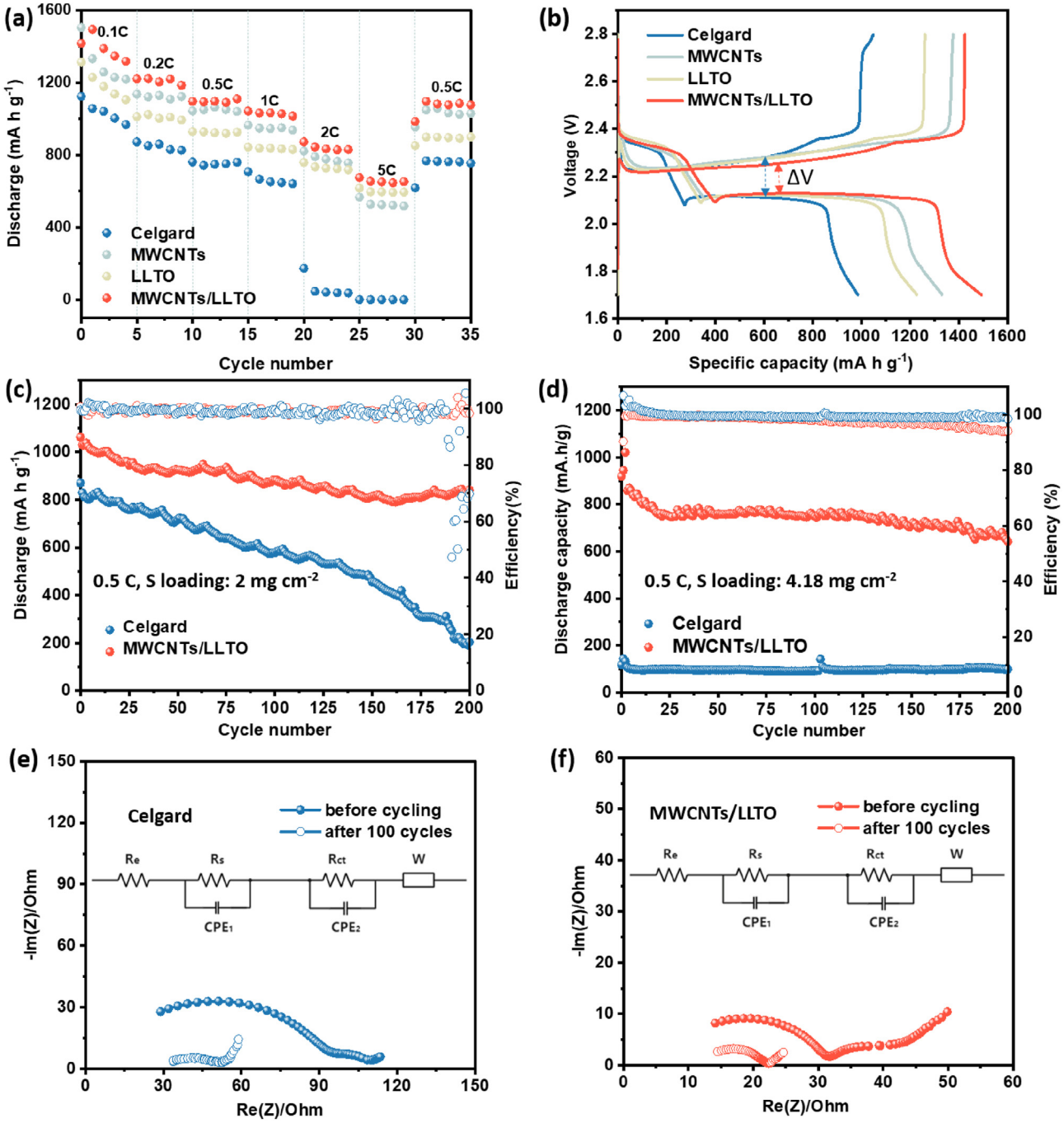

Fig. 4. (a) Rate capability performance of Li-S cells with four different separators: pristine Celgard, MWCNTs, LTTO, and MWCNTs/LTTO-modified separators. (b) Discharge/charge profiles for the initial cycle at 0.1 C. Long cycling properties of Li-S cells adopting a Celgard separator and MWCNTs/LLTO-modified separator. (c) The active mass loading of the S cathode is around 2 mg/cm^2, and (d) the higher active mass loading of the S cathode is around 4.18 mg/cm^2. Electrochemical impedance spectra of (e) Li-S cells with Celgard separator and (f) Li-S cells with MWCNTs/LLTO-modified separator before cycling and after 100 cycles (the cells with S loading of 2 mg/cm^2). The insets in (e) and (f) show the equivalent circuits. MWCNTs/LTTO, multi-walled carbon nanotubes/lithium lanthanum titanium oxide.

showing the largest specific capacity and the smallest overpotential for the cells adopting MWCNTs/LLTO-modified separator. The charge/discharge profiles under different current rates are depicted in Fig. S9. The excellent rate performance of the cells employing the MWCNTs/LLTO-modified separator confirms the importance of fast kinetics occurring over the electrodes in improving the cell performance.

To evaluate the cycling performance of the MWCNTs/LLTO-modified separator vs. pristine Celgard, Li-S cells with a low S loading of 2 mg/cm^2 were tested at 0.5 C (Fig. 4c). The cells with MWCNTs/LLTO-modified separators show a more stable long cycle life (200 cycles) than pristine Celgard, with the specific discharge capacity decreasing from 1029 down to 875 mA/h/g after 100 cycles while still retaining 828 mA/h/g after 200 cycles. From Fig. 4c, it can be noticed that most of the capacity decreases during the first 150 cycles, while a stable behavior is manifested afterward, with a capacity retention rate at 200 cycles as high as 80% and a high Coulombic efficiency (CE) approaching 9 %. On the other hand, the

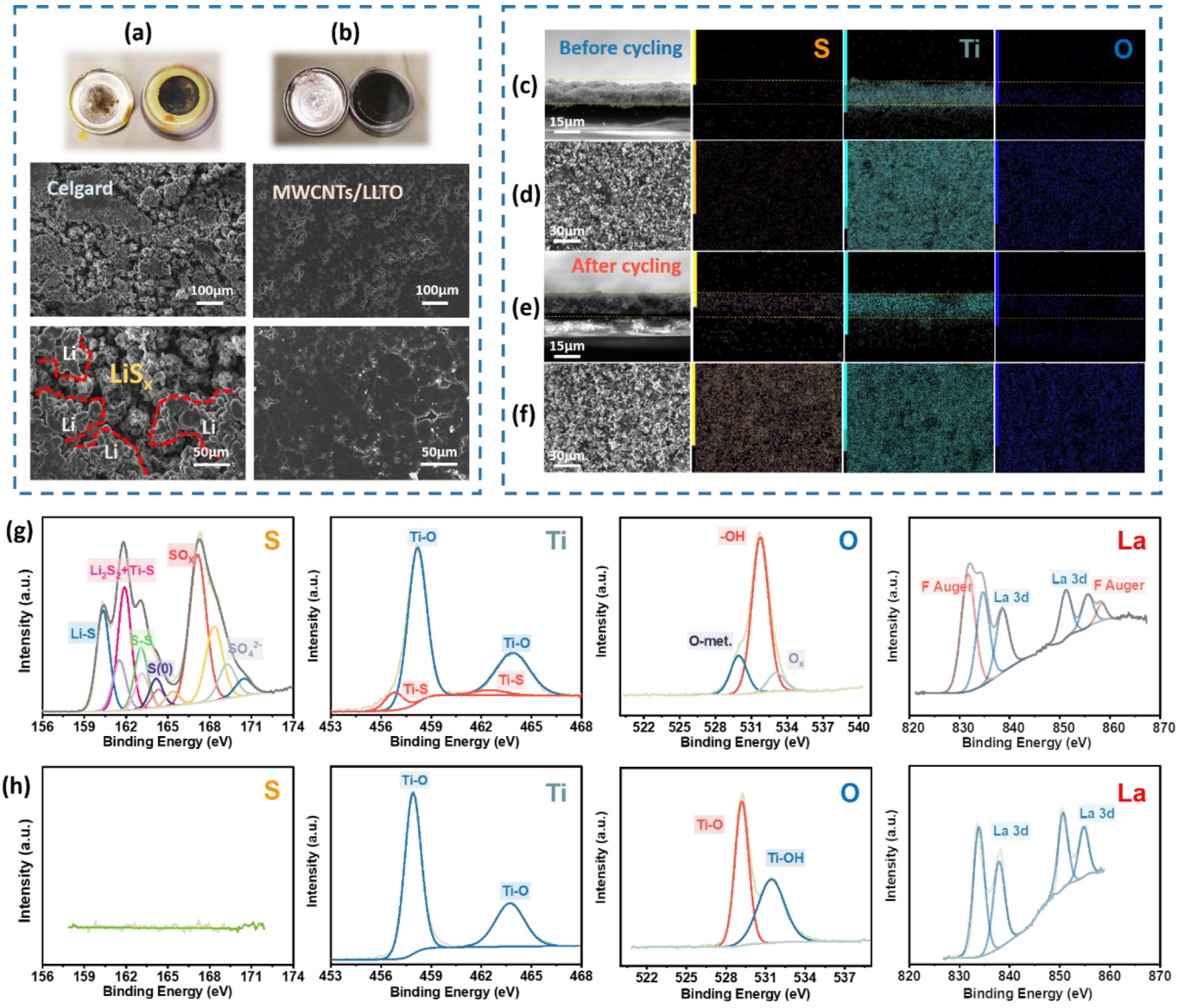

Fig. 5. SEM micrographs at different scales of cycled lithium metal in Li-S cells with (a) pristine Celgard separator and (b) MWCNTs/LLTO-modified separator. From (c) to (f) are shown the SEM micrographs and the elemental maps of the MWCNTs/LLTO-modified separator before cycling and after 100 cycles performed at 0.5 C. In particular, (c) and (d) show the top surface and the cross-section of the separator before cycling, respectively. (e) and (f) show the top surface and the cross-section of the separator after 100 cycles, respectively. The elemental maps describe S with an orange color, Ti with a light-blue color, and O with a blue color. (g) and (h) depict the XPS analysis of the MWCNTs/LLTO-modified separator after cycling at 0.5 C and the XPS analysis of the pristine LLTO powder, respectively. SEM, scanning electron microscopy; MWCNTs/LLTO, multi-walled carbon nanotubes/lithium lanthanum titanium oxide; XPS, X-ray photoelectron spectroscopy.

cells adopting the pristine Celgard separator show a rapid specific capacity drop from the initial 820 mA/h/g down to 230 mA/h/g after 200 cycles, with a low capacity retention of 28%, which comes near 1/3 of the cell containing the MWCNTs/LLTO-modified separator. Furthermore, the associated CE decreases rapidly after 180 cycles, suggesting the occurrence of strong battery degradation when the Celgard separator is employed. When the S loading was doubled from 2 mg/cm^2 up to 4.18 mg/cm^2 and the amount of electrolyte was almost halved (E/S ratio, 6 μL/mg), the cells employing a pristine Celgard separator could hardly perform, with a specific capacity of only 143 mA/h/g at 0.1 C and 102 mA/h/g at 0.5 C (Fig. 4d). In contrast, the cells using MWCNTs/LLTO-modified separators returned much better behavior with the specific capacity slightly decreasing during the first 30 cycles, however, maintaining a very appreciable 750 mA/h/g for 100 cycles. In general, the overall behavior of the MWCNTs/LLTO-modified separator outperforms most reports in the literature, as listed in Table S2.

Fig. 4e and f compare the EIS before and after 100 cycles at 0.5 C, measured for Li-S cells with pristine Celgard (Fig. 4e) and with MWCNTs/LLTO-modified separators (Fig. 4f). Based on the Nyquist plots, the equivalent circuit was determined and inserted in the figures. In this respect, both figures show two semicircles in the impedance spectra before cycling. The large semicircle at the high-frequency region represents the interface resistance (R_s//CPE_1), while the small semicircle at the medium-frequency regions reflects the charge transfer on the positive electrode (R_{ct}//CPE_2). Furthermore, R_e describes the resistance of the electrolyte, and the Warburg impedance (W) is used to represent lithium ion diffusion

within the cathode [45,46]. The total impedance of the cell with a pristine Celgard separator is nearly three times higher than the impedance of the cell with MWCNTs/LLTO-modified separator (108.23 Ω vs. 42.92 Ω). The cells with the MWCNTs/LLTO-modified separator show a more pronounced response in the medium-frequency region (R_{ct}) due to the presence of the MWCNTs/LLTO coating on the separator. This coating introduces more charge transport interfaces in the cathode, thereby increasing the contribution of R_{ct} in the overall cell impedance. After 100 cycles, the cell with MWCNTs/LLTO-modified separator maintains a smaller impedance (22.23 Ω) compared to the cell with a pristine Celgard separator (53.64 Ω), which confirms the efficient suppression of insulating solid sulfur species during cycling. These results reveal that the cells with MWCNTs/LLTO-modified separators possess larger reversibility and smaller passivation than the cells with a pristine Celgard separator, which confirms the aforementioned results about rate capability and cycling performance.

Furthermore, the surface morphology of metallic lithium and S cathode was analyzed after cycling to verify whether any damages had occurred due to the presence of LiPSs [47]. By comparing the surface morphology of the cycled lithium anode, it appears that the cells with a pristine Celgard separator have returned a lithium surface with a high degree of roughness and breakage (Fig. 5a), indicating severe corrosion due to the dissolution of polysulfides into the electrolyte, their migration through the separator, and the consecutive reaction with metallic lithium. On the other hand, the cycled lithium anode in the cells with MWCNTs/LLTO-modified separators displays a clean surface with only lithium metal being visible (Fig. 5b), which suggests a reduced shuttle effect within this kind of cell. This provides further evidence that the MWCNTs/LLTO-modified separator can effectively reduce polysulfide diffusion. Furthermore, the morphological response of the S cathode before and after cycling was also analyzed (Fig. S10). The results show that when the Celgard separator is employed, remarkable damage can be observed, damage due to the conversion from S to Li_2S accompanied by a huge volume expansion. Indeed, the poor reaction kinetics and the limited solid-to-solid conversion in the cells adopting the Celgard separator lead to a large amount of Li_2S accumulating on the electrode surface, hindering electron/ion transport and causing serious damage. However, when the MWCNTs/LLTO-modified separator is considered, the results show a flat and undamaged surface with less accumulated insoluble polysulfide, resulting from improved reaction kinetics due to the presence of an ionic/electronic co-conductive coating.

Fig. 5c–f illustrates the SEM micrographs and elemental maps of the MWCNTs/LLTO-modified separator before and after 200 cycles at 0.5 C. For both Ti and O elements, the maps show a similar morphology as the SEM micrographs obtained before and after cycling, regardless of whether they are observed from the top or through a cross-sectional cut. The situation is instead different when S is observed, as its maps show a complete absence of S before cycling as S was not present in the separator. Vice versa, after a full cycling process (100 cycles in the present case), the S maps show a complete overlap with the corresponding SEM micrographs, demonstrating that the S species are efficiently trapped in the MWCNTs/LLTO coating layer during cycling. Moreover, there are very few orange dots (S) observed in the Celgard layer, indicating that almost no S species could penetrate into the separator. It is possible to affirm that the shuttle effect was significantly suppressed by the usage of the MWCNTs/LLTO-modified separators.

Finally, to achieve a comprehensive understanding of polysulfide conversion during the cycling process, the MWCNTs/LLTO-modified separator after the cycling (Fig. 5g) and the pristine LLTO powder (Fig. 5h) were examined by XPS. While for LLTO no S signal is observed, Fig. 5g demonstrates that the S signal splits into two groups. Above 166 eV, a large number of oxidized S species, including sulfate (BE = 169.29 eV), thiosulfate (BE = 167.15 eV), and polythionates (BE = 168.34 eV), were detected. Below 166 eV, the measurements have instead identified the reduced S species Li_2S (BE = 160.34 eV) and Li_2S_2 (BE = 161.91 eV), the terminal S_0 (BE = 164.16 eV), and the bridged S–S (BE = 163.04 eV) [48]. Furthermore, the Ti–S bonding at approximately 161.4 eV is hidden by the peak of Li_2S_2. When the Ti XPS pattern for the MWCNTs/LLTO-modified separator is observed, it can be noticed that two peaks appear at 456.73 eV and 462.60 eV, peaks that are instead absent in the pristine LLTO powder. These peaks are attributed to the Ti–S bond in the cycled separator, which is a direct consequence of the coupling effect between LLTO and polysulfides. In the O 1s spectrum of the pristine LLTO, the peaks at 529.19 eV and 531.42 eV represent the characteristics of the titanate oxygen (Ti–O) and hydroxyl (–OH) species, respectively. In the corresponding spectrum of the MWCNTs/LLTO-modified separators, the intensity of the –OH peak increases significantly after cycling. The binding energy of the oxide (O_x) peak is fixed at 533.1 eV, which is due to the O–S bond in the oxidized S species mentioned before. Finally, moving to the La spectrum for pristine LLTO, it is observed that it comprises 3D bimodal peaks, which, due to the absorption of LiTFSI from the electrolyte, are modified by the appearance of two additional F Auger peaks at 832.01 eV and 858.20 eV in the MWCNTs/LLTO-modified separator. All in all, the XPS elemental analysis confirms the formation of chemical interactions between the LLTO surface and the S species.

4. Conclusions

In conclusion, the modified separator consisting of an electronic and ionic co-conductive MWCNTs/LLTO layer deposited on commercial Celgard has been effectively produced. On one side, the MWCNTs in the MWCNTs/LLTO-modified separator can physically adsorb soluble polysulfides and provide electron transfer pathways within the MWCNTs/LLTO interlayer, thereby forming a natural connection with the S cathode. This enables the polysulfides to be effectively immobilized and further re-utilized during the discharge process. On the other side, the LLTO does not only form chemical bonds with polysulfides, but it also substantially increases the Li-ion transport number owing to its own excellent ionic conductivity, hence further increasing the lithium diffusion. Consequently, the employment of the MWCNTs/LLTO-modified separator in the Li-S cells leads to a significant inhibition of the shuttle effect, a weakening of the passivation on lithium, and fast redox reaction kinetics during the charge/discharge process. These unique merits ensure that the cells employing the MWCNTs/LLTO-modified separator possess an improved specific capacity, rate capability, and cycling performance than the Li-S cells adopting a pristine Celgard separator. Considering the simple scale-up fabrication process and the good electrochemical performance, the MWCNTs/LLTO-modified separator is expected to have a promising application foreground for high-performance LSBs and other electrochemical applications.

CRediT author statement

Remo Proietti Zaccaria: Funding acquisition, Supervision, Writing – original draft. Marco Ricci: Investigation, Writing – review & editing. Susana Chauque: Visualization, Writing – original draft, Writing – review & editing. Shanshan Liang: Conceptualization, Data

curation, Formal analysis, Methodology, Writing – original draft, Writing – review & editing.

Declaration of competing interest

The authors declare that they have no known competing financial interests or personal relationships that could have appeared to influence the work reported in this paper.

Data availability

Data will be made available on request.

Acknowledgments

The authors gratefully acknowledge the National Natural Science Foundation of China (No. 32071317).

Appendix A. Supplementary data

Supplementary data to this article can be found online at https://doi.org/10.1016/j.mtener.2024.101497.

References

[1] B. Dunn, H. Kamath, J.-M. Tarascon, Electrical energy storage for the grid: a battery of choices, Science 334 (2011) 928–935, https://doi.org/10.1126/science.1221774.
[2] X. Ji, L.F. Nazar, Advances in Li-S batteries, J. Mater. Chem. A 20 (2010) 9821, https://doi.org/10.1039/B925751A.
[3] N. Nitta, F. Wu, J.T. Lee, G. Yushin, Li-ion battery materials: present and future, Mater. Today 18 (2015) 252, https://doi.org/10.1016/j.mattod.2014.10.040.
[4] A. Manthiram, Y. Fu, S.H. Chung, C. Zu, Y.S. Su, Rechargeable lithium-sulfur batteries, Chem. Rev. 114 (2014) 11751, https://doi.org/10.1021/cr500062v.
[5] G. Li, S. Wang, Y. Zhang, M. Li, Z. Chen, J. Lu, Revisiting the role of polysulfides in lithium-sulfur batteries, Adv. Mater. 30 (2018) 1705590, https://doi.org/10.1002/adma.201705590.
[6] Y.V. Mikhaylik, J.R. Akridge, Polysulfide shuttle study in the Li/S battery system, J. Electrochem. Soc. 151 (2004) A1969, https://doi.org/10.1149/1.1806394.
[7] S.S. Zhang, Liquid electrolyte lithium/sulfur battery: fundamental chemistry, problems, and solutions, J. Power Sources 231 (2013) 153, https://doi.org/10.1016/j.jpowsour.2012.12.102.
[8] G. Li, S. Wang, Y. Zhang, M. Li, Z. Chen, J. Lu, Revisiting the role of polysulfides in lithium-sulfur batteries, Adv. Mater. 30 (2018) e1705590, https://doi.org/10.1002/adma.201705590.
[9] S. Dörfler, H. Althues, P. Härtel, T. Abendroth, B. Schumm, S. Kaskel, Challenges and key parameters of lithium-sulfur batteries on pouch cell level, Joule 4 (2020) 539, https://doi.org/10.1016/j.joule.2020.02.006.
[10] H. Li, Y. Li, L. Zhang, Designing principles of advanced sulfur cathodes toward practical lithium-sulfur batteries, SusMat 2 (2022) 34–64, https://doi.org/10.1002/sus2.42.
[11] X.B. Liu, Z.C. Xiao, C.G. Lai, S. Zou, M. Zhang, K.X. Liu, Y.H. Yin, T.X. Liang, Z.P. Wu, Three-dimensional carbon framework as high-proportion sulfur host for high-performance lithium-sulfur batteries, J. Mater. Sci. Technol. 48 (2020) 84, https://doi.org/10.1016/j.jmst.2020.03.001.
[12] S. Zhang, K. Ueno, K. Dokko, M. Watanabe, Recent advances in electrolytes for lithium–sulfur batteries, Adv. Energy Mater. 5 (2015) 1500117, https://doi.org/10.1002/aenm.201500117.
[13] J. Tan, J. Matz, P. Dong, M. Ye, J. Shen, Appreciating the role of polysulfides in lithium-sulfur batteries and regulation strategies by electrolytes engineering, Energy Storage Mater. 42 (2021) 645–678, https://doi.org/10.1016/j.ensm.2021.08.012.
[14] Z. Shen, W. Zhang, S. Mao, S. Li, X. Wang, Y. Lu, Tailored electrolytes enabling practical lithium-sulfur full batteries via interfacial protection, ACS Energy Lett. 6 (2021) 2673–2681, https://doi.org/10.1021/acsenergylett.1c01091.
[15] S. Zhang, K. Ueno, K. Dokko, M. Watanabe, Recent advances in electrolytes for lithium-sulfur batteries, Adv. Energy Mater. 5 (2015) 1500117, https://doi.org/10.1002/aenm.201500117.
[16] Q.N. Zhao, R.H. Wang, J. Wen, X.L. Hu, Z.Y. Li, M.H. Li, F.S. Pan, C.X. Xu, Separator engineering toward practical Li-S batteries: targeted electrocatalytic sulfur conversion, lithium plating regulation, and thermal tolerance, Nano Energy. 95 (2022) 106982, https://doi.org/10.1016/j.nanoen.2022.106982.
[17] Y. Pan, S. Chou, H.K. Liu, S.X. Dou, Functional membrane separators for next-generation high-energy rechargeable batteries, Natl. Sci. Rev. 4 (2017) 917, https://doi.org/10.1093/nsr/nwx037.
[18] H. Yang, C. Guo, A. Naveed, J. Lei, J. Yang, Y. Nuli, J. Wang, Recent progress and perspective on lithium metal anode protection, Energy Storage Mater. 14 (2018) 199–221, https://doi.org/10.1016/j.ensm.2018.03.001.
[19] D. Lin, Y. Liu, Y. Cui, Reviving the lithium metal anode for high-energy batteries, Nat. Nanotechnol. 12 (2017) 194–206, https://doi.org/10.1038/nnano.2017.16.
[20] R. Yi, C. Liu, Y. Zhao, L.J. Hardwick, Y. Li, X. Geng, Q. Zhang, L. Yang, C. Zhao, A light-weight free-standing graphene foam-based interlayer towards improved Li-S cells, Electrochim. Acta. 299 (2019) 479–488, https://doi.org/10.1016/j.electacta.2019.01.015.
[21] S. Tu, X. Chen, X. Zhao, M. Cheng, P. Xiong, Y. He, Q. Zhang, Y. Xu, A polysulfide-immobilizing polymer retards the shuttling of polysulfide intermediates in lithium-sulfur batteries, Adv. Mater. 30 (2018) e1804581, https://doi.org/10.1002/adma.201804581.
[22] H. Shao, W. Wang, H. Zhang, A. Wang, X. Chen, Y. Huang, Nano-Tio_2 decorated carbon coating on the separator to physically and chemically suppress the shuttle effect for lithium-sulfur battery, J. Power Sources 378 (2018) 537–545, https://doi.org/10.1016/j.jpowsour.2017.12.067.
[23] P. Zeng, L. Huang, X. Zhang, Y. Han, Y. Chen, Inhibiting polysulfides diffusion of lithium-sulfur batteries using an acetylene black-CoS_2 modified separator: mechanism research and performance improvement, Appl. Surf. Sci. 427 (2018) 242–252, https://doi.org/10.1016/j.apsusc.2017.08.062.
[24] Z. Shen, X. Jin, J. Tian, M. Li, Y. Yuan, S. Zhang, S. Fang, X. Fan, W. Xu, H. Lu, J. Lu, H. Zhang, Cation-doped ZnS catalysts for polysulfide conversion in lithium–sulfur batteries, Nat. Catal. 5 (2022) 555–563, https://doi.org/10.1038/s41929-022-00804-4.
[25] H. Zhang, R. Dai, S. Zhu, L. Zhou, Q. Xu, Y. Min, Bimetallic nitride modified separator constructs internal electric field for high-performance lithium-sulfur battery, J. Chem. Eng. 429 (2022) 132454, https://doi.org/10.1016/j.cej.2021.132454.
[26] B. Qi, X. Zhao, S. Wang, K. Chen, Y. Wei, G. Chen, Y. Gao, D. Zhang, Z. Sun, F. Li, Mesoporous tin microspheres as an efficient polysulfide barrier for lithium-sulfur batteries, J. Mater. Chem. A 6 (2018) 14359–14366, https://doi.org/10.1039/c8ta04920c.
[27] J.L. Yang, S.X. Zhao, Y.M. Lu, X.T. Zeng, W. Lv, G.Z. Cao, In-situ topochemical nitridation derivative MoO_2-Mo_2N binary nanobelts as multifunctional interlayer for fast-kinetic li-sulfur batteries, Nano Energy. 68 (2020) 104356, https://doi.org/10.1016/j.nanoen.2019.104356.
[28] Z. Xu, Z. Wang, M.R. Wang, H.T. Cui, Y.Y. Liu, H.Y. Wei, J. Li, Large-scale synthesis of Fe_9S_{10}/Fe_3O_4@c heterostructure as integrated trapping-catalyzing interlayer for highly efficient lithium-sulfur batteries, Chem. Eng. J. 422 (2021) 130049, https://doi.org/10.1016/j.cej.2021.130049.
[29] C. Yuan, X.F. Yang, P. Zeng, J. Mao, K.H. Dai, L. Zhang, X.L. Sun, Recent progress of functional separators with catalytic effects for high-performance lithium-sulfur batteries, Nano Energy. 84 (2021) 105928, https://doi.org/10.1016/j.nanoen.2021.105928.
[30] L. Borchardt, M. Oschatz, S. Kaskel, Carbon materials for lithium sulfur batteries-ten critical questions, Chemistry 22 (2016) 7324–7351, https://doi.org/10.1002/chem.201600040.
[31] S.H. Chung, A. Manthiram, Current status and future prospects of metal-sulfur batteries, Adv. Mater. 31 (2019) 1901125, https://doi.org/10.1002/adma.201901125.
[32] H.-J. Peng, J.-Q. Huang, X.-B. Cheng, Q. Zhang, Review on high-loading and high-energy lithium-sulfur batteries, Adv. Energy Mater. 7 (2017) 1700260, https://doi.org/10.1002/aenm.201700260.
[33] J.-Q. Huang, Q. Zhang, F. Wei, Multi-functional separator/interlayer system for high-stable lithium-sulfur batteries: progress and prospects, Energy Storage Mater. 1 (2015) 127–145, https://doi.org/10.1016/j.ensm.2015.09.008.
[34] Y.S. Su, A. Manthiram, A new approach to improve cycle performance of rechargeable lithium-sulfur batteries by inserting a free-standing mwcnt interlayer, Chem. Commun. 48 (2012) 8817, https://doi.org/10.1039/C2CC33945E.
[35] J. Wu, L. Chen, T. Song, Z. Zou, J. Gao, W. Zhang, S. Shi, A review on structural characteristics, lithium ion diffusion behavior and temperature dependence of conductivity in perovskite-type solid electrolyte $Li_{3x}La_{2/3-x}TiO_3$, Funct. Mater. Lett. 10 (2017) 1730002, https://doi.org/10.1142/s179360471730002x.
[36] Y. Inaguma, C. Liquan, M. Itoh, T. Nakamura, T. Uchida, H. Ikuta, M. Wakihara, High ionic conductivity in lithium lanthanum titanate, Solid State Commun. 86 (1993) 689, https://doi.org/10.1016/0038-1098(93)90841-A.
[37] Y. Sun, P. Guan, Y. Liu, H. Xu, S. Li, D. Chu, Recent progress in lithium lanthanum titanate electrolyte towards all solid-state lithium ion secondary battery, Crit. Rev. Solid State Mater. Sci. 44 (2019) 265–282, https://doi.org/10.1080/10408436.2018.1485551.
[38] G.B. Kunshina, O.B. Shcherbina, V.I. Ivanenko, Study of transport properties and microstructure of lithium-conducting $Li_{0.33}La_{0.56}TiO_3$ ceramic, Russ. J. Appl. Chem. 92 (2019) 1351–1358, https://doi.org/10.1134/s1070427219100045.
[39] M.-Y. Wang, S.-H. Han, C.-Q. Niu, Z.-S. Chao, W.-B. Luo, H.-G. Jin, W.-J. Yi, Z.-Q. Fan, J.-C. Fan, Perovskite lithium lanthanum titanate-modified separator as both adsorbent and converter of soluble polysulfides toward high-performance li-s battery, ACS Sustain. Chem. Eng. 8 (2020) 16477–16492, https://doi.org/10.1021/acssuschemeng.0c05295.
[40] C. Susana, G.M. Anderson, P.d.L.B. Ana, G.S. Antonio, H.B. Adriano, M.T. Roberto, Cerium oxide-sulfur nanohybrids: combining the robust adsorption of polysulfides with enhanced redox kinetics to improve the

energy storage capabilities of Li-S batteries, Electrochim. Acta 382 (2021) 138284, https://doi.org/10.1016/j.electacta.2021.138284.
[41] X. Huang, Z. Wang, R. Knibbe, B. Luo, S.A. Ahad, D. Sun, L. Wang, Cyclic voltammetry in lithium-sulfur batteries-challenges and opportunities, Energy Technol. 7 (2019) 1801001, https://doi.org/10.1002/ente.201801001.
[42] S. Zugmann, M. Fleischmann, M. Amereller, R.M. Gschwind, H.D. Wiemhöfer, H.J. Gores, Measurement of transference numbers for lithium ion electrolytes via four different methods, a comparative study, Electrochim. Acta 56 (2011) 3926–3933, https://doi.org/10.1016/j.electacta.2011.02.025.
[43] Y. Liang, J.K.-H. Hui, T. Yamada, N. Kimizuka, Electrochemical thermoelectric conversion with polysulfide as redox species, ChemSusChem 12 (2019) 4014–4020, https://doi.org/10.1002/cssc.201901566.
[44] P. Zhou, X. Zhang, Y. Xiang, K. Liu, Strategies to enhance Li^+ transference number in liquid electrolytes for better lithium batteries, Nano Res. 16 (2023) 8055–8071, https://doi.org/10.1007/s12274-022-4833-1.
[45] Z. Deng, Z. Zhang, Y. Lai, J. Liu, J. Li, Y. Liu, Electrochemical impedance spectroscopy study of a lithium/sulfur battery: modeling and analysis of capacity fading, J. Electrochem. Soc. 160 (2013) A553, https://doi.org/10.1149/2.026304jes.
[46] A. Kilic, D. Eroglu, Characterization of the effect of cell design on Li-S battery resistance using electrochemical impedance spectroscopy, Chemelectrochem 8 (2021) 963–971, https://doi.org/10.1002/celc.202100165.
[47] F. Chu, M. Wang, J. Liu, Z. Guan, H. Yu, B. Liu, F.J.A.F.M. Wu, Low concentration electrolyte enabling cryogenic lithium–sulfur batteries, Adv. Funct. Mater. 32 (2022) 2205393, https://doi.org/10.1002/adfm.202205393.
[48] Y. Li, W. Li, X. Yan, Z. Zhou, X. Guo, J. Liu, C. Mao, Z. Zhang, G. Li, Terminal sulfur atoms formation via defect engineering strategy to promote the conversion of lithium polysulfides, J. Mater. Sci. Technol. 103 (2022) 221–231, https://doi.org/10.1016/j.jmst.2021.06.050.